## **REPORT**

### **SOLAR CELLS**

# **Deterministic fabrication of 3D/2D perovskite bilayer** stacks for durable and efficient solar cells

Siraj Sidhik<sup>1,2</sup>, Yafei Wang<sup>2,3</sup>, Michael De Siena<sup>4</sup>, Reza Asadpour<sup>5</sup>, Andrew J. Torma<sup>6</sup>, Tanguy Terlier<sup>7</sup>, Kevin Ho<sup>8</sup>, Wenbin Li<sup>2,6</sup>, Anand B. Puthirath<sup>1</sup>, Xinting Shuai<sup>1</sup>, Ayush Agrawal<sup>2</sup>, Boubacar Traore<sup>9</sup>, Matthew Jones<sup>1,10</sup>, Rajiv Giridharagopal<sup>8</sup>, Pulickel M. Ajayan<sup>1</sup>, Joseph Strzalka<sup>11</sup>, David S. Ginger<sup>8</sup>, Claudine Katan<sup>9</sup>, Muhammad Ashraful Alam<sup>5</sup>, Jacky Even<sup>12</sup>\*, Mercouri G. Kanatzidis<sup>4</sup>, Aditya D. Mohite<sup>1,2</sup>\*

Realizing solution-processed heterostructures is a long-enduring challenge in halide perovskites because of solvent incompatibilities that disrupt the underlying layer. By leveraging the solvent dielectric constant and Gutmann donor number, we could grow phase-pure two-dimensional (2D) halide perovskite stacks of the desired composition, thickness, and bandgap onto 3D perovskites without dissolving the underlying substrate. Characterization reveals a 3D-2D transition region of 20 nanometers mainly determined by the roughness of the bottom 3D layer. Thickness dependence of the 2D perovskite layer reveals the anticipated trends for n-i-p and p-i-n architectures, which is consistent with band alignment and carrier transport limits for 2D perovskites. We measured a photovoltaic efficiency of 24.5%, with exceptional stability of  $T_{99}$  (time required to preserve 99% of initial photovoltaic efficiency) of >2000 hours, implying that the 3D/2D bilayer inherits the intrinsic durability of 2D perovskite without compromising efficiency.

he progressive increase in the power conversion efficiency (PCE) of solutionprocessed perovskite solar cells (PSCs) (1, 2) has been enabled in part by strategies to passivate the grain boundaries and interfaces between the perovskite absorber and the charge transport layers (3-9). Twodimensional (2D) halide perovskite (HaP) passivation layers, which have been the most effective in improving the open-circuit voltage ( $V_{\rm OC}$ ) and fill factor (FF) (10-13), are commonly grown by spin-coating an organic cation dispersed in isopropyl alcohol or chloroform on top of 3D HaPs (14, 15). This coating removes some excess lead iodide (PbI2) from the 3D perovskite layer to then form heterogeneous

2D phases or ultrathin layers of wide-bandgap 2D HaP (16-18).

These advances have enhanced durability, as demonstrated recently by Azmi et al., using damp-heat tests (19); however, the lack of control over the phase purity, film thickness, orientation, and structural phase of the 2D HaP has limited their use as an interfacial passivation layer (20). A solvent-free growth of the 2D BA<sub>2</sub>PbI<sub>4</sub> perovskite on the 3D film by controlling the pressure, temperature, and time was demonstrated by Jang et al., indicating the importance of a high-quality 3D/2D interface (21). However, such solid-state in-plane growth is difficult to scale to large areas. Thus, the fabrication of solution-processed heterostructures of 3D/2D HaP with the desired energy levels, thickness, and orientation has been lacking.

We report a solvent design principle for fabricating solution-processed 3D/2D HaP bilayer structures with the desired film thickness and phase purity of any 2D HaP-including Ruddlesden-Popper (RP), Dion-Jacobson (DJ), or alternating cation interlayer (ACI)—described by the general formula of  $L'A_{n-1}B_nX_{3n+1}$  (DJ) where L' is a long-chain organic cation, A is a small monovalent cation, B is a divalent metal, X is a monovalent anion, and n is the number of PbI<sub>6</sub> bonded octahedra along the stacking axis. Our approach leverages two essential properties of the processing solvents, the dielectric constant  $(\epsilon_r)$  and the Gutmann donor number  $(D_N)$ , which controls the coordination between the precursor ions and the solvent (22). Processing solvents with dielectric constant  $\varepsilon_r > 30$  and Gutmann number,  $5 < D_N <$ 18 kcal/mol could effectively dissolve the 2D HaP powders without dissolving or degrading

the underlying 3D perovskite film during processing by using spin coating, doctor blading, or slot die coating.

Control over the different n value and film thicknesses allowed us to progressively tune the heterostructure from a type I to a type II, with the 2D perovskites acting as a transport layer. We achieved a PCE of 24.5% with a high  $V_{\rm OC}$  of 1.20 V in a regular n-i-p device using a RP 2D BA<sub>2</sub>MA<sub>2</sub>Pb<sub>3</sub>I<sub>10</sub> perovskite with a thickness of 50 nm. A comparison of the International Summit on Organic Photostability ISOS-L-1 protocol [maximum power point tracking under ambient conditions] stability of 3D/phasepure 2D (PP-2D) HaP bilayer PSC with the 2D-passivated 3D, control-3D, and control-2D PSCs showed that the 3D/PP-2D HaP bilayer device exhibited exceptional stability with  $T_{99}$ (time required to preserve 99% of the initial PCE) > 2000 hours. Thus, these structures had the durability of the 2D perovskite films without compromising PCE (23).

The comprehensive selection criteria for solvents that could selectively dissolve either the 2D or 3D HaP without disrupting the underlying 3D or 2D layer, respectively, were based on the dielectric constant and the Gutmann donor number (Fig. 1A). These two distinct attributes are correlated. The dielectric constant determines the power of a solvent to dissolve any ionic compound by screening the Coulomb attraction between the ions, whereas the Gutmann donor number describes the Lewis basicity of the solvent and measures the extent to which coordination compounds may form between solvent and cations (high donor number) or between the precursors themselves (low donor number) in the absence of competitive binding of the solvent (24, 25). For example, in the precursor solution composed of methylammonium iodide (MAI), formamidinium iodide (FAI), and PbI2 a solvent with a high Gutmann number would strongly coordinate with divalent metal centers (Pb2+) and suppress the formation of molecular clusters {for example, iodoplumbates such as [PbI<sub>6-x</sub>  $(\text{solvent})_x]^{-(4-x)}$ , where  $x \le 6$ } that would otherwise form in a solvent with low Gutmann number. The strength of these interactions determined the differences in the solubility of the 3D and 2D HaP powders in various solvents (Fig. 1A).

Typical vials of RP 2D (BA<sub>2</sub>MAPb<sub>2</sub>I<sub>7</sub>) and the 3D HaP powders (Fig. 1B) illustrate their solubility in different solvents. Polar aprotic solvents (Fig. 1A, green dots) with a dielectric constant > 30, such as N, N-dimethylformamide (DMF) and dimethyl sulfoxide (DMSO), fully dissolved both 3D and 2D HaP. Solvents such as acetonitrile (MeCN), tetramethyl sulfone (TMS), propylene carbonate (PC), and ethylene carbonate (EC) also have a dielectric constant > 30 but did not dissolve the 3D HaP powders because their weak Lewis basicity ( $D_N$  < 18 kcal/mol) made

<sup>1</sup>Department of Material Science and Nanoengineering, Rice University, Houston, TX 77005, USA. <sup>2</sup>Department of Chemical and Biomolecular Engineering, Rice University, Houston, TX 77005, USA. 3School of Mechanical and Electric Engineering, Guangzhou University, Guangzhou, Guangdong 510006, China. <sup>4</sup>Department of Chemistry and Department of Materials Science and Engineering, Northwestern University, Evanston, IL 60208, USA. <sup>5</sup>School of Electrical and Computer Engineering, Purdue University, West Lafayette, IN 47907, USA. 6Applied Physics Graduate Program, Smalley-Curl Institute, Rice University, Houston, TX 77005, USA. <sup>7</sup>Shared Equipment Authority, Secure and Intelligent Micro-Systems (SIMS) Laboratory, Rice University, Houston, TX 77005, USA. <sup>8</sup>Department of Chemistry, University of Washington, Seattle, WA 98195, USA. <sup>9</sup>École Nationale Supérieure de Chimie de Rennes (ENSCR), Univ Rennes, CNRS, Institut des Sciences Chimiques de Rennes (ISCR)-UMR 6226, F-35000 Rennes, France. 10 Department of Chemistry, Rice University, Houston, TX 77005, USA. <sup>11</sup>X-Ray Science Division, Argonne National Laboratory, Argonne, IL 60439, USA. 12 Institut National des Sciences Appliquées (INSA) Rennes, Univ Rennes, CNRS, Institut Fonctions Optiques pour les Technologies de l'Information (FOTON)-UMR 6082, F-35000 Rennes, France. \*Corresponding author. Email: adm4@rice.edu (A.D.M.); jacky.

even@insa-rennes.fr (J.E.)

the formation of Pb<sup>2+</sup> solvent coordination complexes unlikely. However, these solvents completely dissolved the 2D perovskite powders. This difference is consistent with 3D perovskite lattices being more stable and difficult to disrupt with solvents of intermediate  $D_{\rm N}$  than the 2D perovskites and implied the presence of additional favorable interactions of these solvents with the organic spacer cations (readily accessible from the edges of the slabs) that were absent in the 3D perovskites.

We observed that both nonpolar (Fig. 1A, blue dots) and polar protic solvents (Fig. 1A, red dots) did not completely dissolve the 2D HaP powders (Fig. 1B). As controls, we also tested solvents with a high Gutmann number and low dielectric constant, such as tetrahydrofuran ( $D_N$  = 20 kcal/mol,  $\varepsilon_r$  = 7.6), and vice versa, such as nitromethane (NME) ( $D_N$  =  $2.7 \text{ kcal/mol}, \, \epsilon_{\rm r}$  = 35.9), both of which did not dissolve the 2D perovskite powders (figs. S1 and S2). Taken together, these results implied that solvents with a dielectric constant > 30 and the Gutmann number  $5 < D_N < 18 \text{ kcal/mol}$ should enable the fabrication of 3D/2D HaP bilayers without disrupting or degrading the underlying 3D HaP film.

To fabricate 3D/2D HaP bilayers with different phases of 2D perovskite and having desired n values and thicknesses, we tested the solubility of the archetypical RP 2D perovskites  $(BA_2MA_{n-1}Pb_nI_{3n+1}, \text{ with } n = 1 \text{ to } 4) \text{ and other}$ crystal phases such as DJ [(4AMP)MAPb $_2$ I $_7$ ] and ACI [(GA)MA<sub>2</sub>Pb<sub>2</sub>I<sub>7</sub>] in the identified 2D perovskite-selective solvents (Fig. 1C). Because of its high polarity, propylene carbonate dissolved the 2D RP phases better than tetramethyl sulfone or acetonitrile. In general, we observed an overall decrease in the solubility of RP 2D HaPs with increasing n value, from >100 mg/ml for n = 1 to 30 to 40 mg/ml for n =4. The decrease in the solubility as a function of increasing n value was consistent with the increase in inorganic lattice fraction of the 2D HaP as the n value approached 3D composition.

In addition, the n = 2 ACI and DJ perovskites exhibited low solubilities of 20 to 40 mg/ml and 10 to 25 mg/ml, respectively, which was consistent with the structure of ACI and DJ 2D perovskites, which was near that of 3D with short interlayer cations that reflected the role of organic spacer cations in the dissolution process. Of all the target solvents, the high volatility of MeCN [boiling point (b.p.) ≈ 82°C] compared with those of the others-such as TMS (b.p.  $\approx 285$ °C), PC (b.p.  $\approx 242$ °C), and EC (b.p. ≈ 248°C)-made it attractive for lowtemperature processing without affecting the stability of the entire stack (figs. S3 and S4 and movies S1 and S2). We focused on the solvent MeCN for fabricating the targeted 3D/2D HaP bilayer.

The protocols for fabricating the 3D/2D HaP bilayer by use of spin coating, drop-casting,

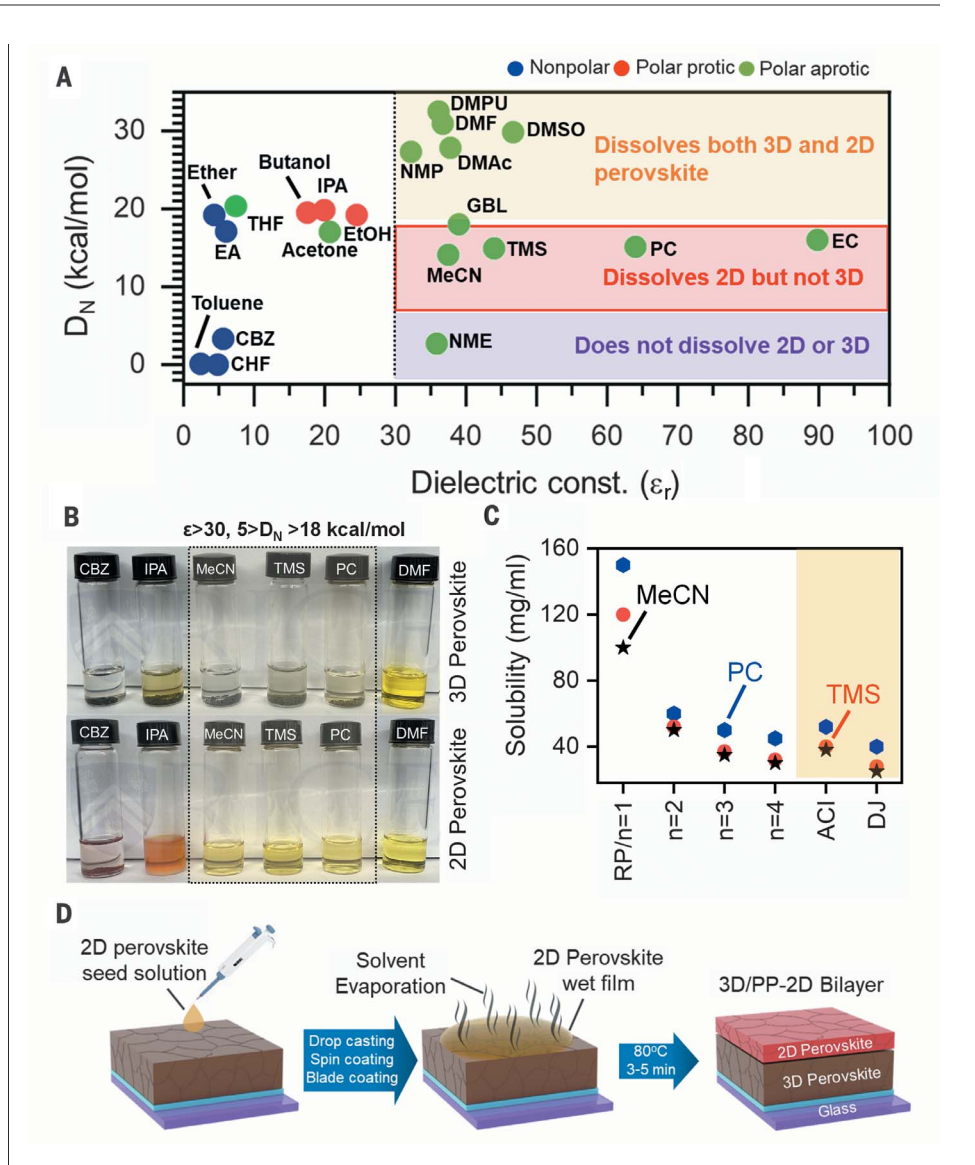


**Fig. 1. Design principle for fabricating a solution-processed 3D/PP 2D HaP bilayer stack.** (**A**) Plot showing different solvents based on the dielectric constant ( $ε_r$ ) and the Gutmann number ( $D_N$ ) to identify the differences in solubility of the 3D and 2D perovskite powders for making a 3D/2D bilayer stack. (**B**) Optical images of 2D (RP BA<sub>2</sub>MAPb<sub>2</sub>I<sub>7</sub>) and 3D perovskite powders in different solvents. (**C**) Solubility of RP BA<sub>2</sub>MA<sub>n-1</sub>Pb<sub>n</sub>I<sub>3n+1</sub> (n=1 to 4), DJ. (4AMP)MAPb<sub>2</sub>I<sub>7</sub>, and ACI, (GA)MA<sub>2</sub>Pb<sub>2</sub>I<sub>7</sub>-based 2D perovskites (where BA is butylamine, MA is methylammonium, AMP is aminomethyl piperidine, and GA is guanidinium) in the solvents MeCN, TMS, and PC as shown. (**D**) Fabrication steps of a 3D/2D HaP bilayer stack. CHF, chloroform; CBZ, chlorobenzene; EA, ethyl acetate; IPA, isopropyl alcohol; NMP, *N*-methyl pyrrolidone; NME, nitromethane; DMF, dimethylformamide; MeCN, acetonitrile; DMAc, dimethylacetamide; GBL, γ-butyrolactone; TMS, tetramethylene sulfone; THF, tetrahydrofuran; DMSO, dimethyl sulfoxide; PC, propylene carbonate; EC, ethylene carbonate; DMPU, *N*,*N*'-Dimethylpropyleneurea.

blade coating, or slot-die coating (Fig. 1D) followed our recent work on obtaining PP-2D HaP films. We created a stable dispersion of 2D perovskite seed solution by dissolving the parent crystal powders in MeCN (fig. S5 and supplementary text) (26, 27). In general, other than the solvents with Gutmann number  $5 < D_{\rm N} < 18$  kcal/mol, any Pb<sup>2+</sup>-weakly coordinating solvents such as DMF, GBL, and DMAc compared with DMSO can produce a dispersion of 2D perovskite seed solution. The precursor solution

with 2D perovskite seeds was coated on top of a 3D HaP layer  $[Cs_{0.05}(MA_{0.10}FA_{0.85})Pb(I_{0.90}Br_{0.10})_3]$  and then annealed at  $80^{\circ}C$  for 5 min. We also used other scalable techniques such as doctor blading, drop-casting, and blade-coating (fig. S6) to demonstrate the industrial viability of the process. By controlling the concentration and deposition technique, we tuned the thickness of the 2D perovskite layer on top of the 3D film ranging from sub–10 nm to submicrometer scales (fig. S7).

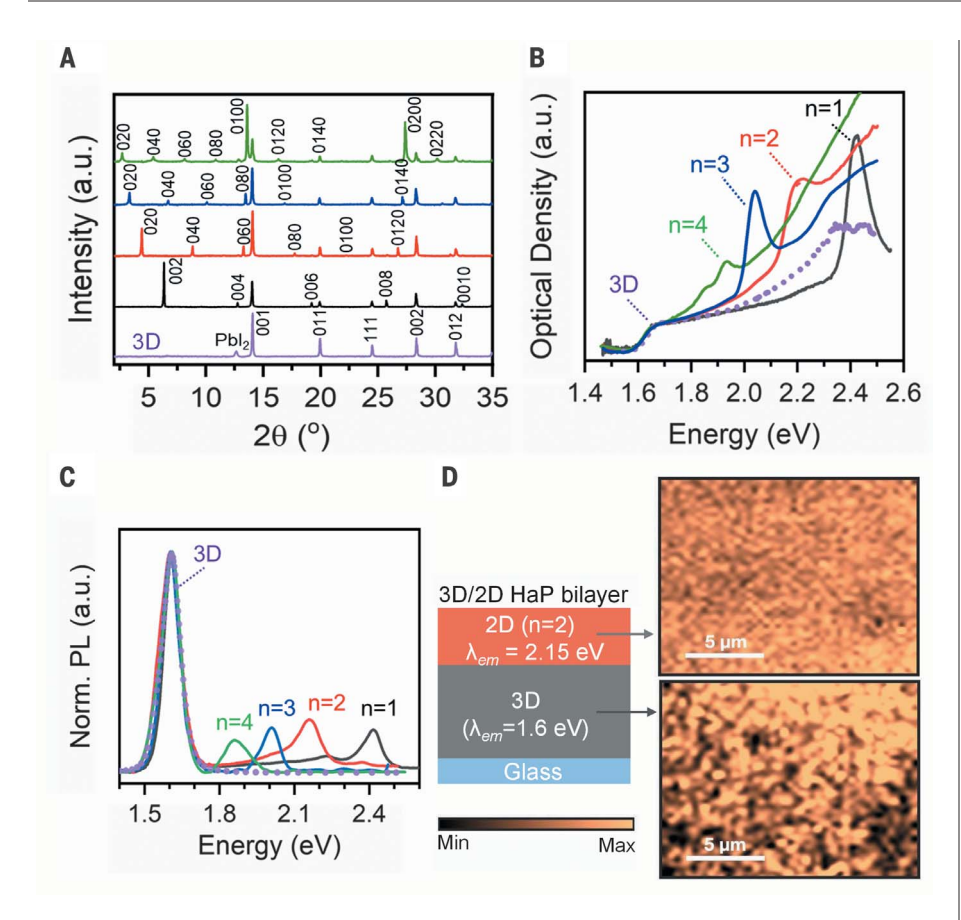


Fig. 2. Structural and optical spectroscopic characterization of 3D and 3D/PP-2D HaP bilayers with n=1 to 4. (A) X-ray diffraction pattern from control 3D  $Cs_{0.05}(MA_{0.10}FA_{0.85})Pb(I_{0.90}Br_{0.10})_3$  and 3D/PP-2D  $(BA_2MA_{n-1}Pb_n|_{3n+1}; n=1$  to 4, 100 nm) stack. (B) Optical absorbance spectra of 3D HaP film and 3D/PP-2D HaP bilayers for RP  $BA_2MA_{n-1}Pb_n|_{3n+1}$  (n=1 to 4) identified through the excitonic peak. (C) PL spectra of 3D and 3D/PP-2D  $(BA_2MA_{n-1}Pb_n|_{3n+1}; n=1$  to 4, 100 nm) HaP bilayer measured with excitation at 480 nm and 360 Watts/cm² with emission from 3D band edge and 2D HaP from n=1 to 4. (D) Schematic diagram depicting the 3D/2D  $(BA_2MAPb_2l_7)$  bilayer stack with the measured confocal PL map centered at the 3D emission peak (1.6 eV), and at 2D emission peak (2.15 eV) showing uniform coverage of the 2D layer and the underlying 3D layer.

Using the design approach described in Fig. 1, we fabricated a 3D/2D HaP [RP  $BA_2MA_{n-1}Pb_nI_{3n+1}$ (n = 1 to 4)] bilayer stack and characterized its phase purity using x-ray diffraction (XRD), optical absorbance, and photoluminescence (PL) techniques. The XRD pattern for the control-3D and 3D/2D HaP bilayers with different 2D RP  $BA_2MA_{n-1}Pb_nI_{3n+1}$  perovskite (n = 1 to 4) (Fig. 2A), matching the low-angle Bragg peaks with the corresponding simulated patterns suggested that the overlying 2D HaP layer had high phase purity (fig. S8). The phase purity was further confirmed with absorbance (Fig. 2B) and PL (Fig. 2C) measurements. The optical absorbance revealed the presence of a 3D HaP band-edge at 1.6 eV for the control film, which was accompanied by a sharp excitonic peak varying from 2.4 eV (n = 1) to 1.9 eV (n = 4) corresponding to the different n values in the 3D/2D bilayer. The steady-state PL measurements further confirmed the phase purity of the 3D/2D HaP bilayers. We did not observe any change in the bandgap of the underlying 3D HaP, indicating that the presence of the 2D HaP layer did not disrupt the 3D perovskite.

To further assess the spatial homogeneity of the 3D/2D HaP bilayer, we monitored the PL emission centered at the 3D peak (1.6 eV) and the 2D peak (n=2,2.15 eV) using confocal microscopy (Fig. 2D). We observed a uniform emission over a large area of 20 by 20  $\mu$ m from the 2D as well as the underlying 3D HaP layer, confirming the homogeneity of the 3D/2D HaP bilayer stack. These measurements indicated that we had grown highly crystalline PP-2D HaP of varying n values on the 3D surface. This fabrication process also worked well with the pure FAPbI<sub>3</sub> and MAPbI<sub>3</sub> 3D HaP, demonstrating its broad applicability (fig. S9).

We used several techniques to characterize the interface between the 3D and PP-2D layers. The time-of-flight secondary ion mass spectrometry (TOF-SIMS) depth profile of the control 3D (Fig. 3A) and 3D/PP-2D HaP bilayer (Fig. 3B) revealed the distribution of ions as a function of film thickness. Upon introduction of BA<sub>2</sub>MAPb<sub>2</sub>I<sub>7</sub> 2D perovskite layer on top of the 3D film, in addition to the Cs<sub>2</sub>I<sup>+</sup> and Cs<sub>2</sub>Br<sup>+</sup> ions and CH<sub>5</sub>N<sub>2</sub><sup>+</sup> (FA<sup>+</sup>) cations, we observed higher intensity of the C<sub>4</sub>H<sub>12</sub>N<sup>+</sup> (BA<sup>+</sup>) compared with the background BA+ intensity (supplementary text) and CH<sub>6</sub>N<sup>+</sup> (MA<sup>+</sup>) ions. These ions were uniformly distributed for a thickness of 50 nm, after which there was a sharp decrease in the concentration. Fitting the change in intensity of the BA+ to the background (representing no BA) yielded an interface transition of 20 nm from the top 2D layer to the underlying 3D HaP. The TOF-SIMS measurements of the 3D|PP-2D (RP BA<sub>2</sub>MA<sub>2</sub>Pb<sub>3</sub>I<sub>10</sub>) bilayer stack show similar results (fig. S10).

The grazing incidence wide-angle x-ray scattering (GIWAXS) spectra of the 3D/PP-2D HaP bilayer for different incident angles (or depth) (Fig. 3, C and D) shows the presence of horizontal oriented BA2MAPb2I7 2D HaP on the surface ( $\alpha = 0.08^{\circ}$ ) and the 3D  $HaP (Cs_{0.05}(MA_{0.10}FA_{0.85})Pb(I_{0.90}Br_{0.10})_3]$  in the form of rings at the bottom ( $\alpha = 0.5^{\circ}$ ) (fig. S11 and supplementary text). This result is well correlated with the calculated x-ray penetration depth curve for the RP-2D HaP, showing a critical angle ( $\alpha_c$ ) of 0.181° (Fig. 3E) (28, 29). The integrated area under the (020) peak (2D signature feature) and the (111)/(001) peak (3D signature feature) from the GIWAXS spectra for various incident angles (0° to 0.5°) (Fig. 3F) revealed the 3D/PP-2D interface at an incident angle of 0.2°. The integrated area under the (020) peak became invariant, whereas the (111)/(001) increased, which confirmed the presence of a 2D HaP layer with a thickness of 50 to 60 nm stacked on top of the 3D HaP film as estimated from the penetration depth curve. The BA2MA2Pb3I10 2D HaP shows a mixed orientation in the 3D/PP-2D (n = 3, RP) HaP bilayer stack with similar interfacial characteristics (detailed GIWAXS analysis is available in fig. S12). The presence of some texture in the same orientation as in the n = 3, RP perovskite is required for efficient charge transfer through the 2D perovskite, resulting in the efficient 3D/PP-2D bilayer HaP solar cells (Fig. 4) (26, 27). The dark-field crosssectional high-resolution transmission electron microscopy (HR-TEM) image of the 3D/ PP-2D (RP BA<sub>2</sub>MAPb<sub>2</sub>I<sub>7</sub>) HaP bilayer grown on the silicon substrate (with gold and carbon as the top protective layer) (Fig. 3G) verified the homogeneity of the 2D HaP laver on top of the 3D HaP thin film. The average intensity profile (Fig. 3G, red) showed an interfacial 3D/PP-2D sharpness of 20 nm, which was consistent with the TOF-SIMS measurements and matched the roughness of the control-3D film (fig. S13). The HR-TEM image of the 3D/PP-2D (RP  $BA_2MA_2Pb_3I_{10}$ ) HaP

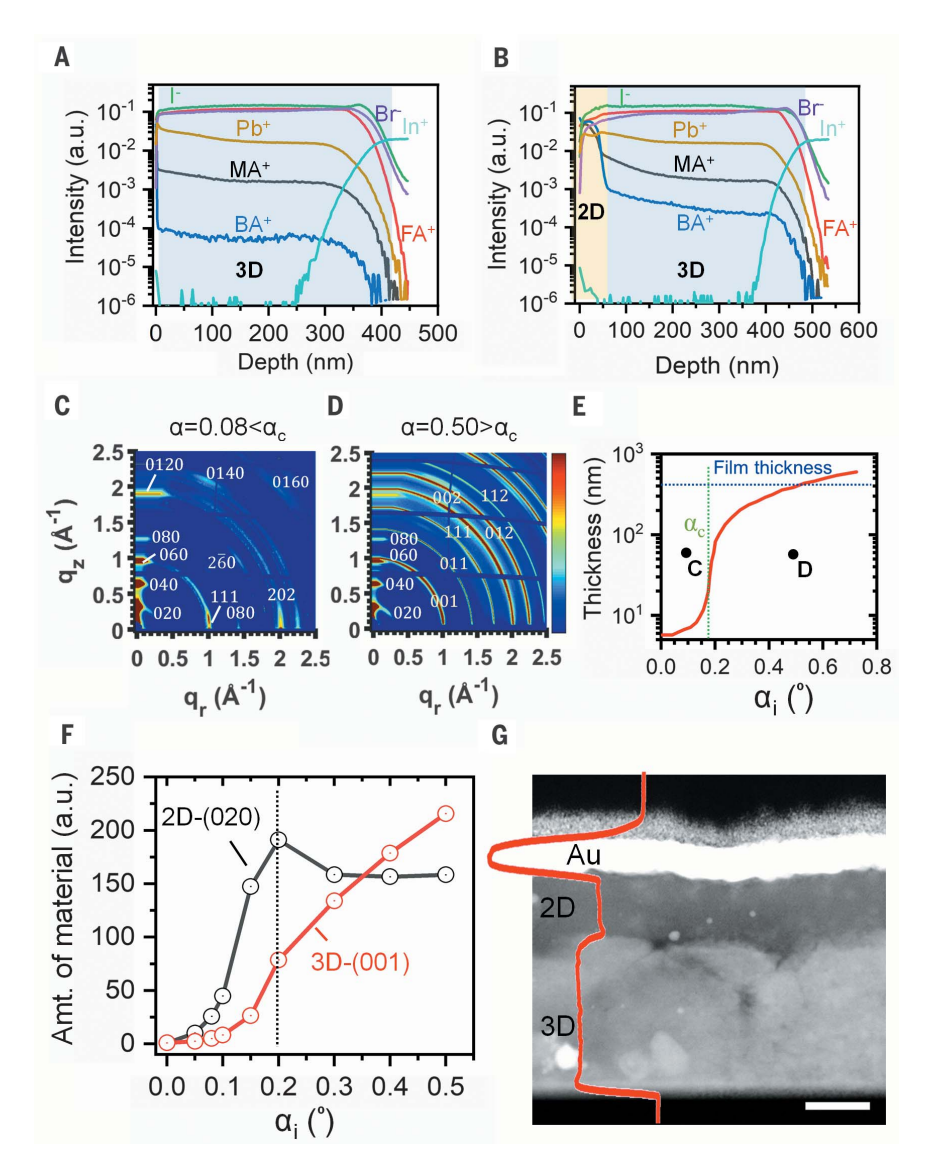


**Fig. 3. 3D/PP-2D HaP interface characterization.** (**A** and **B**) ToF-SIMS depth profiles of the (A) control  $Cs_{0.05}(MA_{0.10}FA_{0.85})Pb(I_{0.90}Br_{0.10})_3$  3D perovskite film and (B) 3D/PP-2D (BA<sub>2</sub>MAPb<sub>2</sub>I<sub>7</sub>) HaP stack deposited on top of indium tin oxide show the distribution of different ions across the thickness and the sharpness of the heterointerface. (**C** and **D**) Angle-dependent GIWAXS pattern of the 3D/PP-2D (RP BA<sub>2</sub>MAPb<sub>2</sub>I<sub>7</sub>) HaP stack shows evolution of 2D and 3D perovskites for increasing incident angle. The most efficient 3D/PP-2D HaP solar cell was obtained for BA<sub>2</sub>MA<sub>2</sub>Pb<sub>3</sub>I<sub>10</sub> RP perovskite, which exhibited mixed vertical orientation (Fig. 4). (**E**) Simulated x-ray penetration depth curve for the RP-2D HaP at various incident angles showing the critical angle and the thickness of the probed film. (**F**) Amount of 2D and 3D HaP materials extracted from the angular integrated diffraction peaks. (**G**) Cross-sectional dark-field HR-TEM image of the 3D/PP-2D (BA<sub>2</sub>MAPb<sub>2</sub>I<sub>7</sub>) HaP stack with the overlaying intensity profile (red) shows transition width from 3D to 2D of 20 nm. Scale bar, 100 nm.

bilayer stack also showed similar interfacial characteristics (fig. S14). All of these results demonstrated that our solvent design strategy allowed for the fabrication of 3D/PP-2D bilayers with a high-quality interface without destroying or altering the crystallinity of the underlying 3D perovskite.

We fabricated solar cells with the 3D/PP-2D HaP bilayer perovskites and measured their performance and durability. We first created an energy-level diagram for the 2D HaP, RP

 $BA_2MA_{n-1}Pb_nI_{3n+1}$  (n=1 to 4), with the 3D perovskite  $Cs_{0.05}(MA_{0.10}FA_{0.85})Pb(I_{0.90}Br_{0.10})_3$  (Fig. 4A) according to values predicted from first-principles calculations (fig. S15) and corroborated with photoemission yield spectroscopy (PES) and absorption measurements (30) (figs. S16 to S18). We observed a type II band alignment between the 3D and the n=3 2D HaP with a near-perfect alignment of valence band edges for 3D and 2D HaP, which is ideal for extracting holes but presents a large energy

barrier for electrons (fig. S19). The 3D/PP-2D (n=1,n=2) HaP bilayer stack shows a type I alignment, which was further confirmed by fabricating solar cells showing a barrier for charge extraction using higher thicknesses of the corresponding 2D layers (supplementary text and fig. S20). As a result, we fabricated n-i-p PSCs with the architecture FTO/SnO<sub>2</sub>/3D/PP-2D (n=3)/spiro-OMeTAD/Au, controlling the PP-2D (n=3) HaP thickness by spin-coating different concentrations of 2D perovskite solution in MeCN (fig. S21).

The current-voltage (I-V) characteristics for three selected thicknesses of 2D HaP layers are shown in Fig. 4B, with 3D HaP as the control. For n-i-p cells, increased 2D HaP thickness from 0 to 50 nm increased  $V_{\rm OC}$  from 1.09 to 1.20 V. This increase in the  $V_{\rm OC}$  was accompanied by a slight increase in the FF from 0.80 to 0.84, and even a small increase in  $J_{SC}$  from 23.54 to 24.34 mA/cm<sup>2</sup> resulting in a peak PCE of 24.5% for a 2D HaP thickness of 50 nm with no hysteresis (figs. S22 and S23). The PCE as a function of 2D HaP thickness shows that increasing the 2D HaP thickness beyond 50 nm decreased the overall PCE (Fig. 4C). We attributed this decrease in PCE to the reduced transport of the free charge carriers from 3D to the 2D HaP limited by the <100 nm diffusion length for a polycrystalline 2D n = 3, RP HaP film with mixed orientation (31, 32) (PV statistics are provided in fig. S23). However, the p-i-n devices with ITO/PTAA/3D/PP-2D(n = 3)/C60/ BCP/Cu exhibited an increase in PCE for a 2D HaP thickness of 5 nm, which is consistent with recent studies of 2D/3D interfaces with an ultrathin 2D layer passivation followed by a drastic decrease for higher thicknesses of 2D HaP (Fig. 4C, black curve, and figs. S24 and S25) (33, 34). The reduction in PCE was consistent with the energy band diagram (Fig. 4A and fig. S19B), which showed a large barrier to electron collection in the p-i-n geometry.

To understand the increase in PV parameters ( $J_{SC}$ ,  $V_{OC}$ , and FF) of the 3D/PP-2D HaP bilayer solar cells, we performed optical and self-consistent transport modeling to simulate the PV characteristics that are supported by the surface photovoltage (SPV), steady-state PL, and time-resolved PL measurements. The optical modeling revealed that the 2D HaP layer increased the photogeneration of the bilayer stack and improved  $J_{\rm SC}$  (fig. S26). This result was consistent with the observed increase in the  $J_{SC}$  by 1.5 mA/cm<sup>2</sup> as we went from the 3D control to the champion 3D/PP-2D HaP bilayer device, validated by external quantum efficiency (EQE) measurements shown in Fig. 4D and the change in EQE ( $\Delta$ EQE) between them (figs. S27 and S28 and supplementary text).

The self-consistent transport simulation predicted reduced recombination at the 3D/HTL interface after the introduction of a 2D HaP layer, improving the  $V_{\rm OC}$  and FF (fig. S29). To

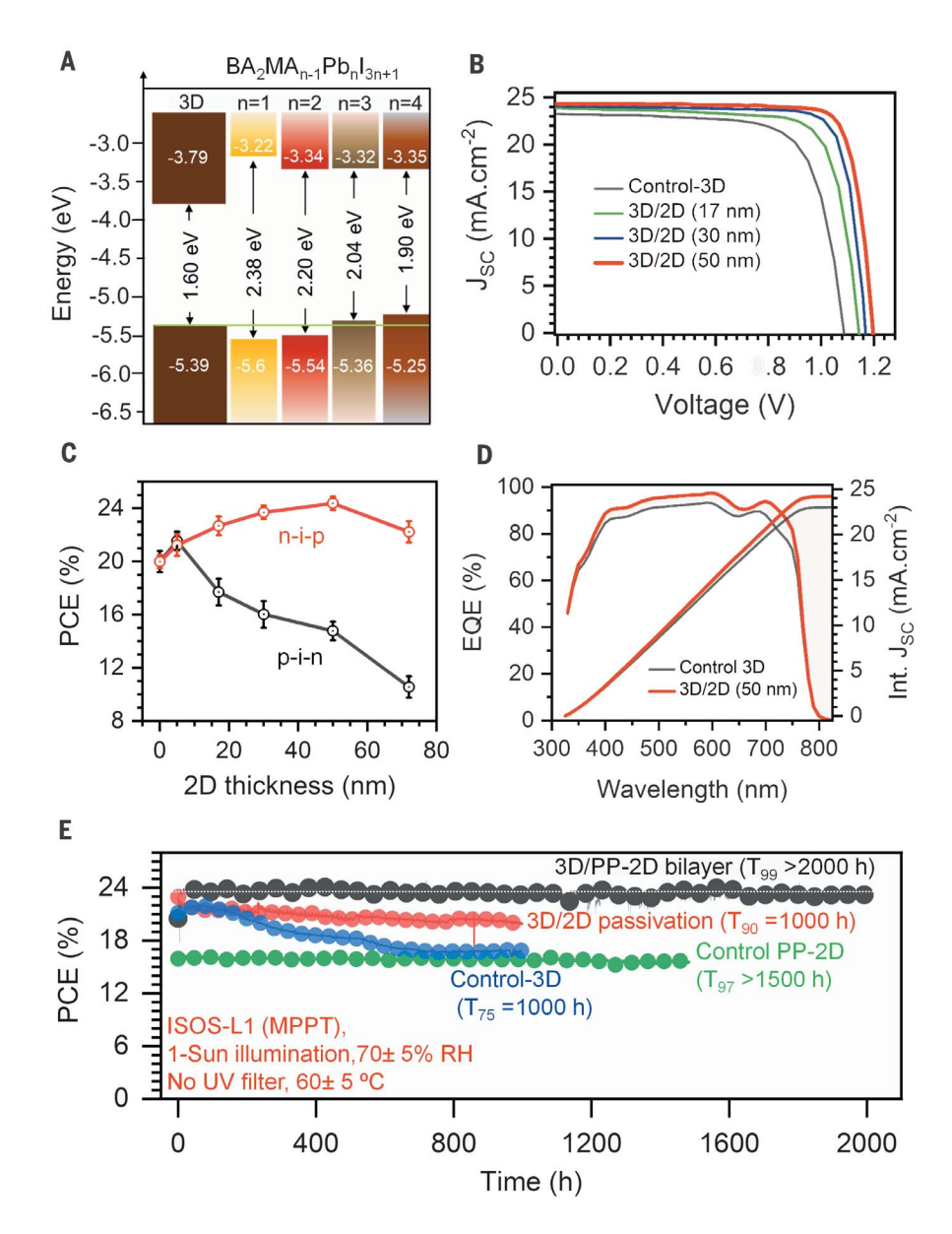


Fig. 4. Photovoltaic performance and long-term stability of the 3D/PP-2D (BA<sub>2</sub>MA<sub>2</sub>Pb<sub>3</sub>l<sub>10</sub>) HaP bilayer solar cells. (A) Energy-level alignment for different n values ( $n \le 4$ ) of 2D perovskite with the 3D perovskite layer with an error of  $\pm 0.05 \text{eV}$ . (B) Current-voltage (l-V) curves of the champion 3D/PP-2D n-i-p PSCs as a function of the 2D layer thickness obtained by spin coating different concentration of the 2D perovskite solution in MeCN. (C) Variation in PCE of the n-i-p and p-i-n planar 3D/PP-2D PSCs as a function of 2D perovskite layer thickness. (D) External quantum efficiency of the device with and without the 2D layer, showing the absorption and current generation ability of the stack. (E) ISOS-L-1 stability measured at maximum power point tracking in ambient condition under continuous 1-sun illumination (55°C) for an epoxy encapsulated PSC. The initial PCE of the control device is 21%; that of the 3D/2D passivated device is 22.93%; that of the 3D/PP-2D bilayer PSC is 23.75%; and that of the PP-2D perovskite device is 16.3%.

corroborate these results, we measured the surface photovoltage (SPV) using scanning Kelvin probe microscopy (SKPM) on the ITO/ SnO\_2/3D/PP-2D (RP BA\_2MA\_2Pb\_3I\_10) stack, which showed an increase in the SPV as a function of the 2D layer thickness (figs. S30 and S31). This result suggested an increase in the quasi-Fermi level separation related to the  $V_{\rm OC}$  of the device

(35–38). The dark I-V curve traces of the solar cells further confirm the increase in  $V_{\rm OC}$  (supplementary text and fig. S32). Additionally, the steady-state PL and time-resolved photoluminescence (TRPL) measurements on the ITO/SnO<sub>2</sub>/3D/PP-2D (RP BA<sub>2</sub>MA<sub>2</sub>Pb<sub>3</sub>I<sub>10</sub>) stack showed enhanced PL emission and increased charge carrier lifetime up to a 2D HaP thickness of

50 nm (fig. S33) but decreases for the higher thickness of 2D HaPs. The overlaying 2D HaP minimized the nonradiative recombination pathways between the 3D perovskite/electrode interface as confirmed by the transport modeling measurements, improving both the FF and the  $V_{\rm OC}$  of the 3D/PP-2D devices (15, 39).

We tested the long-term operational stability of our 3D/PP-2D bilayer encapsulated device following the ISOS-L-1 protocol (Fig. 4G) (23). After 2000 hours of continuous illumination, the 3D/PP-2D HaP bilayer device showed negligible degradation with  $T_{99} > 2000$  hours, whereas the control 3D device lost 25% of its initial PCE. As controls, we also measured the stability of the 3D PSC passivated with a spin-coated organic cation, butylammonium iodide, and compared it with our 3D/PP-2D PSCs using the same conditions. The 2D HaP passivated 3D PSCs show a 10% loss of efficiency after 1000 hours of continuous operation, which is consistent with other recent reports (4, 19). We also measured a pure 2D HaP control device, which showed a  $T_{97} > 1500$  hours, implying that the 3D/PP-2D bilayer perovskite has acquired the inherent stability of the 2D perovskite material.

## REFERENCES AND NOTES

- J. Jeong et al., Nature 592, 381–385 (2021)
- 2. H. Min et al., Nature 598, 444-450 (2021).
- 3. Q. Jiang et al., Nat. Photonics 13, 460-466(2019).
- 4. F. Zhang et al., Science 375, 71–76 (2022).
- 5. X. Zheng et al., Nat. Energy 5, 131–140 (2020).
- 5. Y. Liu et al., Sci. Adv. 5, eaaw2543 (2019).
- 7. N. K. Noel et al., ACS Nano **8**, 9815–9821 (2014).
- D. W. deQuilettes et al., ACS Energy Lett. 1, 438–444 (2016).
- 9. I. L. Braly et al., Nat. Photonics 12, 355-361 (2018).
- 10. A. A. Sutanto et al., Chem 7, 1903-1916 (2021).
- 11. G. Wu et al., Adv. Mater. 34, e2105635 (2022).
- 12. G. Li et al., ACS Energy Lett. 6, 3614-3623 (2021).
- M. A. Mahmud et al., Adv. Funct. Mater. 32, 2009164 (2022).
- 14. E. Jokar et al., ACS Energy Lett. 6, 485–492 (2021).
- 15. J. J. Yoo et al., Energy Environ. Sci. 12, 2192-2199 (2019).
- 16. T. Zhang et al., Joule **2**, 2706–2721 (2018). 17. P. Li et al., Adv. Mater. **30**, e1805323 (2018).
- 18. F. Wang et al., Joule **2**, 2732–2743 (2018).
- 19. R. Azmi et al., Science **376**, 73–77 (2022).
- 20. M. Xiong et al., ACS Energy Lett. 7, 550-559 (2022).
- 21. Y.-W. Jang et al., Nat. Energy 6, 63-71 (2021).
- 22. V. Gutmann, Coord. Chem. Rev. 18, 225-255 (1976).
- 23. M. V. Khenkin et al., Nat. Energy 5, 35-49 (2020).
- 24. J. C. Hamill Jr., J. Schwartz, Y.-L. Loo, ACS Energy Lett. 3, 92–97 (2017).
- J. C. Hamill Jr. et al., J. Phys. Chem. C 124, 14496–14502 (2020).
- 26. S. Sidhik et al., Adv. Mater. 33, e2007176 (2021).
- 27. S. Sidhik et al., Cell Rep. Phys. Sci. 2, 100601 (2021).
- M. Tolan, M. Tolan, X-Ray Scattering From Soft-Matter Thin Films: Materials Science and Basic Research (Springer, 1999), vol. 148.
- 29. R. M. Kennard *et al.*, *Chem. Mater.* **33**, 7290–7300 (2021).
- 30. I. Spanopoulos et al., J. Am. Chem. Soc. **141**, 5518–5534 (2019).
- 31. M. Seitz et al., Nat. Commun. 11, 2035 (2020).
- 32. E. D. Kinigstein et al., Mater. Lett. 2, 1360-1367 (2020).
- 33. M. Degani *et al.*, *Sci. Adv.* **7**, eabj7930 (2021).
- 34. X. Wang et al., Nat. Commun. 12, 52 (2021).
- S. Kavadiya et al., in 2020 47th IEEE Photovoltaic Specialists Conference (PVSC) (IEEE, 2020), pp. 1439–1440.
- 36. I. Levine et al., Joule 5, 2915-2933 (2021).

37. L. Kronik, Y. Shapira, *Surf. Sci. Rep.* **37**, 1–206 (1999). 38. R. Giridharagopal *et al.*, *ACS Nano* **13**, 2812–2821 (2019).

39. J. Wang et al., ACS Energy Lett. **4**, 222–227 (2018).

### **ACKNOWLEDGMENTS**

We thank M. H. K. Samani and A. B. Marciel for useful discussions on the DLS measurements. Funding: The work at Rice University was supported by the DOE-EERE 0008843 program. J.E. acknowledges the financial support from the Institut Universitaire de France and GENCI national computational resources. The work at ISCR and Institut FOTON was performed with funding from the European Union's Horizon 2020 research and innovation program under grant agreement 861985 (Pero CUBE). At Northwestern, the work was supported by the Office of Naval Research (ONR) under grant N00014-20-1-2725. This research used facilities of the Advanced Photon Source, a US Department of Energy (DOE) Office of Science User Facility operated for the DOE Office of Science by Argonne National Laboratory under contract DE-ACO2-06CH11357. ToF-SIMS analysis were carried out with support provided by the National Science Foundation CBET-1626418. This work was conducted in part using resources of

the Shared Equipment Authority at Rice University. The work at the University of Washington by K.H., R.G., and D.S.G. is supported by DOE BES under award DE-SC0013957. This research used facilities and instrumentation supported by the US National Science Foundation through the UW Molecular Engineering Materials Center (MEM-C), a Materials Research Science and Engineering Center (DMR-1719797). Author contributions: A.D.M., S.S., and J.E. conceived the idea, designed the experiments, analyzed the data, and cowrote the manuscript, S.S. and Y.W. studied different solvents. Y.W. performed 2D/3D passivation experiments with S.S.; W.L. and J.S. performed GIWAXS measurements, A.J.T. performed PL maps, X.S. performed SEM and AFM imaging, and A.A. helped with solar cell fabrication and characterization. M.D. performed photoluminescence measurements, M.G.K. and M.J. analyzed the solvation chemistry along with synthesis of 2D HaP crystals. C.K. and B.T. helped understand the 3D/2D interface with DFT modeling. A.B.P. and P.M.A. performed focused ion beam milling (FIB) and electron microscopy (TEM and STEM). K.H., R.G., and D.S.G. performed SKPM and TRPL measurements, R.A. and M.A.A. performed device modeling and optical simulations. T.T. helped perform TOF-SIMS and analyze data. All authors contributed to the manuscript. Competing interests: Rice University have filed patent for method of fabricating the 3D/PP-2D bilayer stack. Data and materials availability: All data are available in the main text or the supplementary materials. License information: Copyright © 2022 the authors, some rights reserved; exclusive licensee American Association for the Advancement of Science. No claim to original US government works. https://www.science.org/about/science-licenses-journal-article-reuse

### SUPPLEMENTARY MATERIALS

science.org/doi/10.1126/science.abq7652 Materials and Methods Supplementary Text Figs. S1 to S33 Tables S1 to S8 References (40–70) Movies S1 and S2

Submitted 2 May 2022; accepted 18 August 2022 10.1126/science.abq7652